

The Importance of Subsurface Residual Stress in Laser Powder Bed Fusion IN718

Itziar Serrano-Munoz, Alexander Evans, Tatiana Mishurova, Maximilian Sprengel, Thilo Pirling, Arne Kromm, and Giovanni Bruno*

The residual stress (RS) in laser powder bed fusion (LPBF) IN718 alloy samples produced using a 67°-rotation scan strategy is investigated via laboratory X-ray diffraction (XRD) and neutron diffraction (ND). The location dependence of the strain-free (d_0) lattice spacing in ND is evaluated using a grid array of coupons extracted from the far-edge of the investigated specimen. No compositional spatial variation is observed in the grid array. The calculated RS fields show considerable non-uniformity, significant stress gradients in the region from 0.6 to 2 mm below the surface, as well as subsurface maxima that cannot be accounted for via XRD. It is concluded that failure to determine such maxima would hamper a quantitative determination of RS fields by means of the stress balance method.

a single build job, thereby allowing significant savings of raw material and substantial reduction of production steps.^[3–5] Laser powder bed fusion (LPBF) is one variant of AM, where the information provided by a sliced 3D-digital model of the component is used to selectively melt a thin layer of metallic powder by means of a high-energy laser beam. Compared with some other AM techniques, LPBF has the advantage of unparalleled freedom of design, minimal feed-stock waste, and high-dimensional accuracy. However, LPBF processing is known to introduce in the as-built parts high residual stress (RS), even close to the yield strength, which possesses complex spatial distributions.

1. Introduction

Inconel 718 (IN718) is a nickel-based superalloy extensively used by the aerospace and power generation industries due to its excellent mechanical performance and corrosion resistance at operating temperatures up to 650 °C.^[1] In addition, the good weldability, high price of the raw material and high tool-wear rates make IN718 alloy an attractive candidate for additive manufacturing (AM).^[2] In fact, AM techniques have gathered considerable popularity in recent years due to their unequalled ability to produce intricate near-net shape parts in


Such RS is typically tensile at the surface and balanced by compression in the bulk. RS results from the repeated localized melting and rapid solidification induced by the laser source.^[6,7] As the build-up of RS has a high dependence on the process parameters (e.g., scan strategy), considerable experimental and numerical efforts have been dedicated to the control and mitigation of RS by optimizing the processing conditions.^[8–12] In particular, surface/subsurface RS maxima (which are the largest),^[13–15] often in combination with defects inherent to the processing,^[16] are seen as the most dangerous for the structural integrity of parts.^[17–19] Subsurface triaxial RS is the most challenging to be determined in a nondestructive fashion: laboratory X-rays can penetrate only few microns, whereas synchrotron X-rays (depths of ≈ 50 – 100 μm) mostly yield RS in only two directions. In contrast, neutron diffraction (ND) yields bulk triaxial stress fields with a good spatial resolution and can be adapted to determine subsurface RS.

Nevertheless, the determination of the bulk triaxial RS state using ND, requires a reliable determination of the strain-free lattice spacing (d_0),^[20] which is not straightforward in AM materials.^[21] The d_0 spatial variation (usually observed in weldments) is mostly induced by changes in the chemical composition.^[22] Most commonly, small coupons (extracted from the very same investigated specimen) are used to measure the reference lattice spacing, assuming that the cutting process does not alter the microstructure of the material.^[23] Another possibility to determine d_0 is to impose stress balance (SB) across a selected cross section of the specimen. This method is ideal when one can assume little chemical variation across the section, i.e., a single global value of d_0 . However, the method requires a detailed map of the lattice spacing across the section, and in particular at the surface and in the subsurface regions, where the largest

I. Serrano-Munoz, A. Evans, T. Mishurova, M. Sprengel, A. Kromm, G. Bruno
Division 8.5
Bundesanstalt für Materialforschung und –prüfung (BAM)
Unter den Eichen 87, Berlin 12205, Germany
E-mail: itziar.serrano-munoz@bam.de

T. Pirling
Diffraction Group (DIF)
Institut Laue-Langevin
71 avenue des Martyrs, CS 20156, Grenoble cedex 9 38042, France

G. Bruno
Institute of Physics and Astronomy
University of Potsdam
Karl-Liebknecht-Str.24-25, Potsdam 14476, Germany

 The ORCID identification number(s) for the author(s) of this article can be found under <https://doi.org/10.1002/adem.202100895>.

© 2021 The Authors. Advanced Engineering Materials published by Wiley-VCH GmbH. This is an open access article under the terms of the Creative Commons Attribution License, which permits use, distribution and reproduction in any medium, provided the original work is properly cited.

DOI: 10.1002/adem.202100895

macroscopic RS (i.e., Type I^[24]) gradients are supposed to occur. This particularity of AM components represents a striking difference to conventionally manufactured structures,^[13,21,25,26] and tailored ND methodologies need to be defined for AM to correctly determine d_0 .

We have observed that using mechanical filings for d_0 determination is unreliable.^[27] We also carried out laboratory X-ray diffraction (XRD) measurements over the cross-sectional perimeter to impose SB over the section.^[27] However, it was clear that a detailed examination of the subsurface RS gradient and its impact on the accuracy of the SB calculation was still missing. This is the objective of this letter.

2. Results and Discussion

An EOS M290 machine from Siemens AG (Power and Gas Division, Berlin, Germany) was used to produce the investigated specimen; its geometry is shown in **Figure 1a**. Virgin (i.e., not recycled) IN718 alloy powder was used to produce prisms by LPBF. Each layer was rotated by an angle of 67° to the subjacent one, and a strip width (i.e., hatch spacing) of 75 μm was used. A lateral offset of 50 mm between subsequent layers was used (Figure 1b). To improve surface finishing, the top surface underwent an up-skin printing process (corresponding to the last three layers, $\approx 120 \mu\text{m}$ thickness), where the volumetric energy density

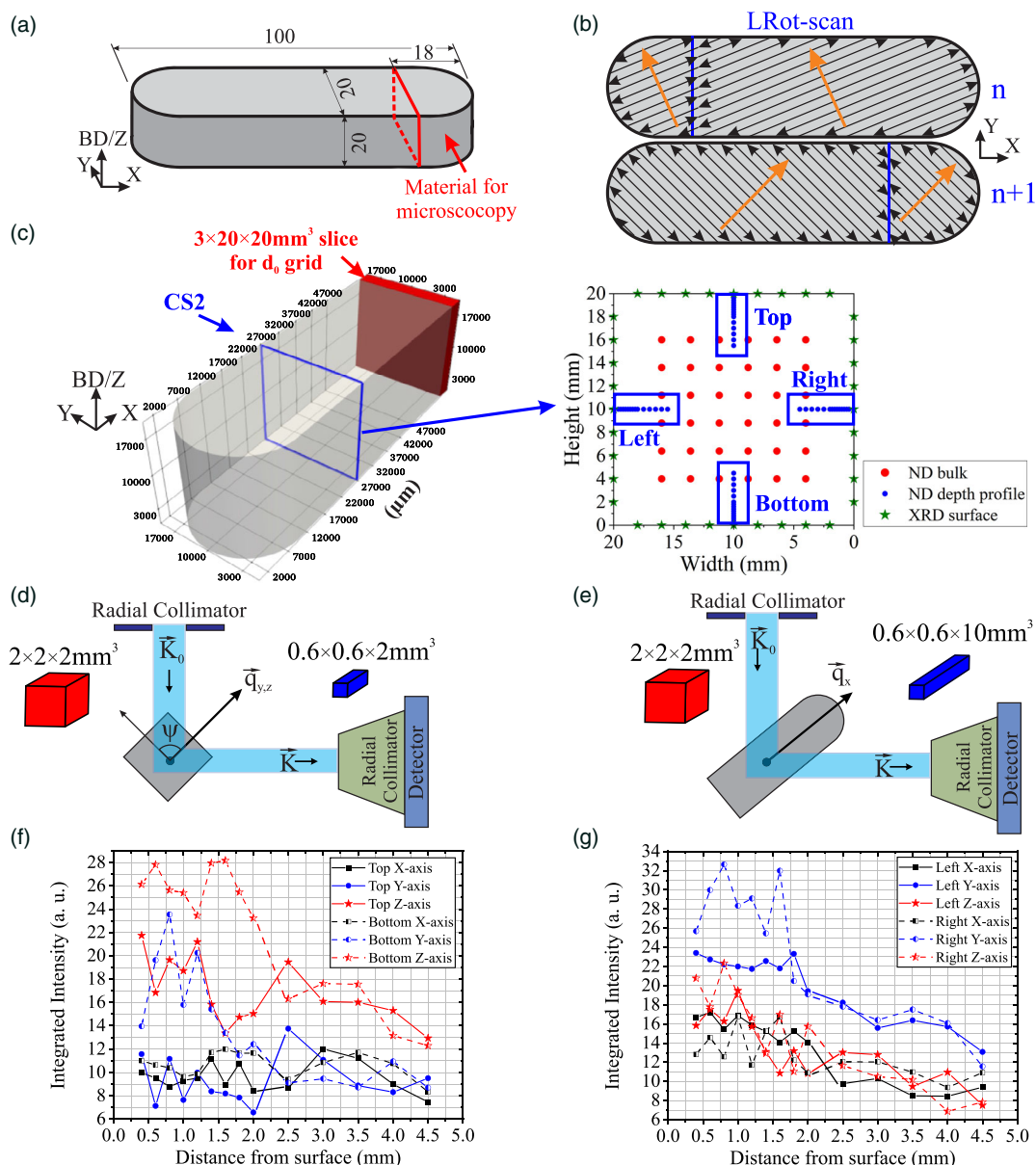


Figure 1. a) Geometry of the sample (dimensions in millimeters). b) Schematic illustration of the 67°-rotation scan strategy, labelled as LRot-scan. c) Left: 3D rendering of the final geometry used for ND; Right: plot describing the location of the measurement points. Schematic illustration of the ND setup d) for measurement of the Y and Z components and e) for the X component. Integrated intensity versus depth for all three components f) in the top and bottom regions and g) in the left and right regions.

was 4% lower than that used in the rest of the specimen. Prior to the diffraction evaluation, a chunk was removed from the specimen for electron microscopy analysis (see Figure 1a). The 67°-rotation processing generated an elongated and crescent-shaped grain morphology with their major axis preferentially parallel to the building direction (BD), as well as a low texture index ($1.1 \times \text{random}$).^[13,27] Also, the specimen was released from the baseplate by means of electrodischarge machining (EDM). To avoid the EDM influence (known to induce high tensile RS^[6]) in the subjacent material, and reliably carry out laboratory XRD analysis, the bottom surface was ground with abrasive SiC papers and subsequently electropolished.

The ND experiments were carried out on the SALSA diffractometer of the ILL (Institute Laue Langevin, Grenoble, France).^[28,29] The specimen was removed from the baseplate and the final length (X axis) after both the extraction of the microscopy sample and the d_0 slice was 78 mm (Figure 1c). An Eulerian cradle combined to the hexapod manipulator allowed automated sample positioning. The investigated gauge volume (GV) was defined by radial focusing collimators. The size of the GV depended on the location of the points (bulk or subsurface). All strain components were measured using a GV of $2 \times 2 \times 2 \text{ mm}^3$ for the bulk points (Figure 1d,e). For depth scans (i.e., subsurface points), the Y and Z strain components were

measured with a $0.6 \times 0.6 \times 2 \text{ mm}^3$ GV, and the X component with a $0.6 \times 0.6 \times 10 \text{ mm}^3$ one (Figure 1d,e) to increase statistics. The YZ -cross section (labeled CS2) located at $X = 27 \text{ mm}$ was scanned on a matrix of 6×6 points (pitch of 2.4 mm) in the bulk. In addition, four depth profiles were run in the subsurface region (0.4–4.5 mm depth) (Figure 1c right, the depth profiles are labeled top, left, bottom, and right) with a step size of 0.5 mm in the 4.5–2 mm region, and 0.2 mm in the region between 2 and 0.4 mm distance to the surface. The Ni(311) lattice plane was used (recommended by ISO standard 21 432,^[30] thanks to its negligible intergranular strain and high multiplicity^[31]) with a neutron beam wavelength of $\lambda = 1.708 \text{ \AA}$. The diffraction elastic constants (DECs) used for RS calculation correspond to those determined by the Reuß model (Young's modulus $E = 178 \text{ GPa}$ and Poisson's ratio $\nu = 0.34$). The choice of Reuß model for LPBF IN718 can be justified by the textured microstructure.^[13] The lattice spacing was calculated by fitting the diffraction peak with a Gaussian function using the ILL in-house developed software LAMP.

The integrated intensity variation in the subsurface regions is shown in Figure 1f,g. Some measurements (e.g., top Z axis) show increased scatter, mainly in the region 2–0.4 mm. Such scatter is lower than 25%; according to Huchings et al.^[32] this implies a texture variation. The last measurement point

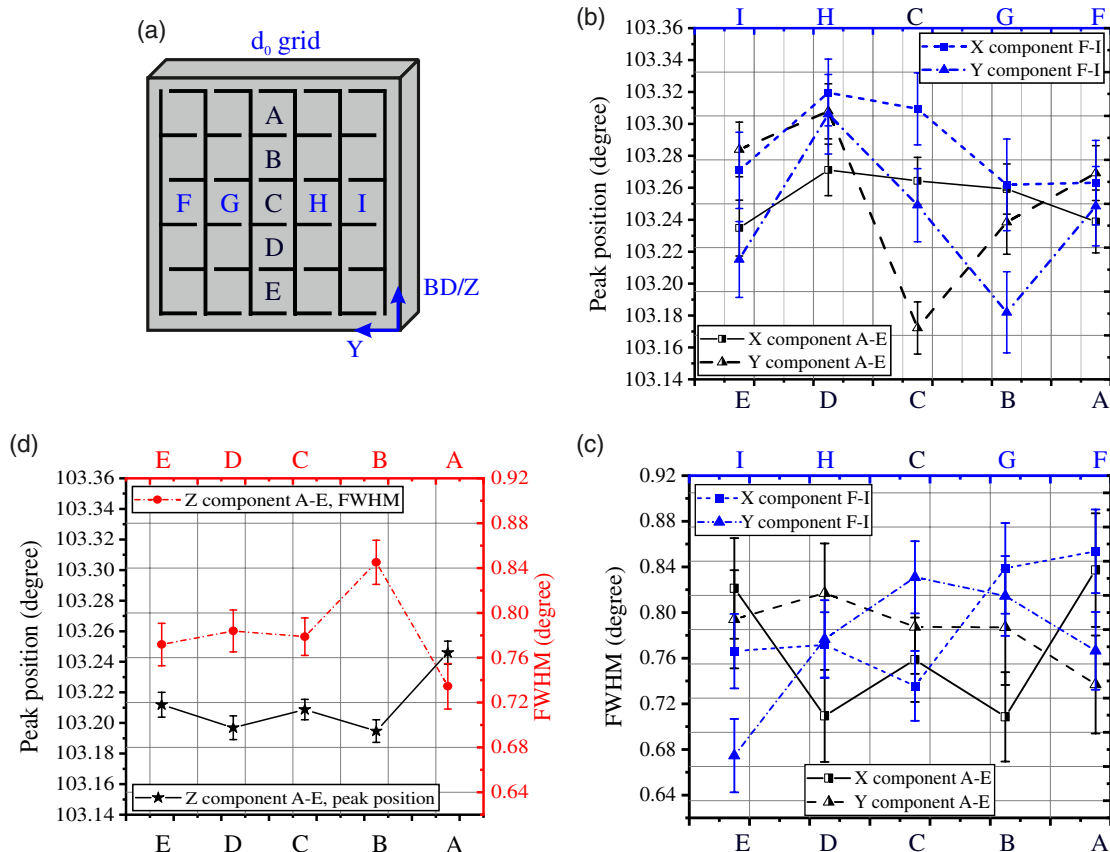


Figure 2. a) Schematic illustration of the d_0 coupon grid. Only the cubes labeled with a letter were investigated. b) Peak position and c) FWHM for the A–E (black half-filled symbols) and F–I (blue filled symbols) array of cubes (X and Y components). d) Peak position and FWHM for the A–E array of cubes (Z component).

(0.4 mm from the surface) is considered as the last point with fully immersed GV (given that the central half the of the GV rhombus diagonal yields more than 80% of the diffracted intensity^[33]). Closer to the surface, pseudostrain corrections are necessary due to partial immersion of the gauge volume.^[34] In this study, the large dimensions of the investigated IN718 specimen render impracticable the reliable use of partial immersion methods, due to a poor signal-to-noise ratio in the subsurface region.

The coupons for the determination of d_0 were produced by extracting a 3 mm slice out of the specimen prior to the ND measurements (the slice location is indicated in Figure 1c). The slice was further stress relieved by creating a grid of cubes of $3 \times 3 \times 3 \text{ mm}^3$ (interlinked by a thin band of material) produced using EDM (see Figure 2a). This method was also used by other authors

(see, e.g., the study by Pant et al.^[35]). In total, nine coupons were investigated, corresponding to the A–E vertical and F–I horizontal central arrays. The X and Y components (lines A–E and F–I) were measured using a $0.6 \times 0.6 \times 2 \text{ mm}^3$ GV, whereas the Z component (lines A–E) using a $2 \times 2 \times 2 \text{ mm}^3$ GV. The peak position exhibits considerable scatter (Figure 2b). Nevertheless, the scatter does not follow any recognizable trend as the one identified, for instance, in the study by Wang et al.^[36] The values of the full width at half maximum (FWHM) also show considerable scatter without a discernible trend (Figure 2c,d). Hence, we can assume that a d_0 spatial variation associated with macro segregation of the alloying elements does not occur in the investigated material. The high scatter (above all in the X and Y directions) is rather attributed to the small GV size compared with the coupon size (the

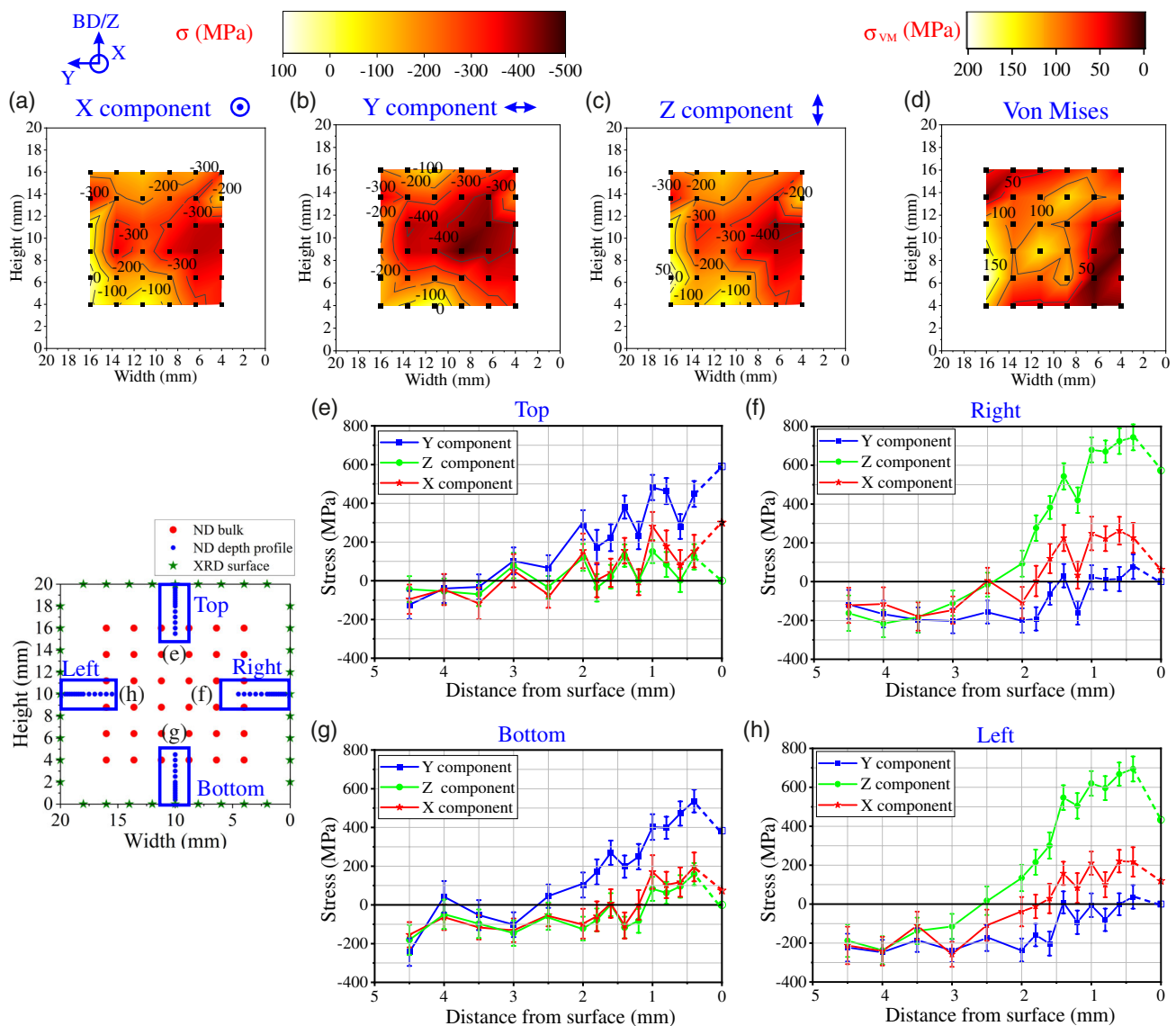


Figure 3. RS maps of the bulk of the specimen for a) the X component, b) the Y component, c) the Z component, and d) the VM equivalent. The average error is $\pm 38 \text{ MPa}$. RS depth profiles of the subsurface points corresponding to e) the top region, f) the right region, g) the bottom region, and h) the left region. Note that the connection to XRD RS values is indicated with dashed lines.

macrostress is not completely averaged out), most probably in combination with local intergranular strain effects. The $2\theta_0$ (peak position of the reference) value was obtained by taking the average of all small GV ($2\theta_0 = 103.25^\circ \pm 0.02^\circ$) and large GV ($2\theta_0 = 103.21^\circ \pm 0.01^\circ$) measurements. The lack of an apparent d_0 spatial variation is in agreement with recent investigations carried out using the same alloy and processing.^[35,37]

RS values were calculated using Hooke's formulae for the quasi-isotropic case. RS fields are highly non-uniform, and values are always compressive in the bulk. Moreover, the minima of all RS components do not lie in the center (Figure 3a–c). Instead, the minimum is shifted to the right ($Y = 7$ mm) and gradients are anisotropic. The highest compressive values (in excess of -450 MPa) are observed in the Y direction. The RS of X and Z components shows similar distributions. The contour plot of the von Mises (VM) RS is even more inhomogeneous (Figure 3d), with the largest values (>100 MPa) along one of the diagonals of the cross section.

At the sample top, we can hypothesize a limited influence of the solid-state thermal cycling: the intrinsic heat treatment of the non-equilibrium microstructure due to cyclic heating and cooling during processing leads to RS fluctuation in the 0.4 – 2 mm region (Figure 3e). In contrast, the bottom layers would endure longer intrinsic heating times, leading to the development of a more uniform stress fields (Figure 3g).^[38,39] In the case of the lateral surfaces (Figure 3f,h), the depth profiles show flat RS profiles in the 0.4 – 1.4 mm region, with a marked fluctuation occurring at 1.2 mm. This feature could be correlated to a change in the direction of the heat flux and grain growth, from a building direction dominance toward a thickness (Y axis) preference.^[13]

To apply stress balance conditions (for σ_x within CS2), the RS state over the perimeter of CS2 was measured with XRD using the $\sin^2\psi$ -method. In our case, the XRD penetration depth is about $5 \mu\text{m}$ (we used Mn $K\alpha$ radiation^[13]). To apply SB, it was necessary to interpolate between the surface and the bulk RS values. The interpolation grid had a 2 mm pitch, equal to the size of the GV used in ND bulk measurements. It is observed that the RS values calculated with SB (see Figure 4a) are about 100 MPa lower than those obtained using the d_0 average from Figure 2d.

The explanation for this difference lies in the presence of subsurface RS maxima (Figure 3e–h). At the top surface, given that the RS is higher than that observed at 0.4 mm depth (≈ 550 MPa against ≈ 450 MPa in the case of σ_x , see Figure 3e), we can assume that the up-skin processing does not induce any maximum below the surface. At the bottom (Figure 3g), however, the RS maximum is expected to occur between 5 and $400 \mu\text{m}$ depth, indicating that, upon removal, a relaxation of the material adjacent to the baseplate might occur. In addition, the lateral surfaces exhibit some degree of surface roughness, which leads to a RS relaxation in the vicinity of the surface (see sketch in Figure 4b). Two studies on LPBF IN718, using the hole-drilling strain-gauge method^[15] and neutron Bragg edge strain scanning,^[14] showed that the location of the subsurface maxima varies considerably, between 0 and 0.6 mm depth. It is also reported that the maximum subsurface value of σ_x can reach up to ≈ 300 MPa.^[14] In our case, we consider that there is not a maximum but rather a region (0.4 – 1.4 mm) where the highest σ_x tensile (≈ 200 MPa) values are observed.

The transition between the ≈ 100 MPa (on average) RS values measured at the surface and the subsurface 200 MPa is expected to occur at some point between 5 and $400 \mu\text{m}$. When inserting the subsurface values in the plot of Figure 3a instead of the XRD data, the SB calculation yields different RS values. The results of such calculation are shown in Figure 4c. With this assumption, the calculated RS values, as well as the reference value ($2\theta_{0,SB} = 103.218^\circ$) becomes similar to those obtained experimentally (Figure 2d). Therefore, we conclude that when subsurface RS maxima are considered, SB becomes a reliable tool for the determination of the strain-free reference d_0 or a validation tool of the accuracy of an experimentally determined d_0 value.

Assuming that the magnitudes of the RS component normal to surfaces can be considered negligible (see Figure 3e–h), we also conclude that coupons, even with the high scatter shown in Figure 2a, can give a reliable estimate of the strain-free lattice spacing when statistically relevant measurements are carried out. Nevertheless, it must be noted that the d_0 value measured along the Z axis in the A coupon (Figure 2d) is significantly different

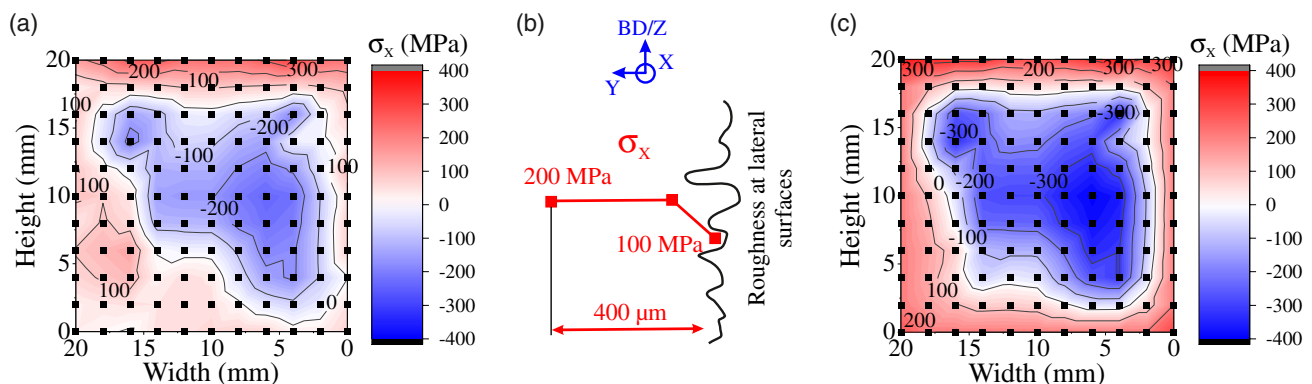


Figure 4. a) σ_x map of CS2 calculated by SB using ND and XRD data (the black squares indicate the location of the interpolation points). b) Schematic illustration of the effect of subsurface RS maxima on the evolution of σ_x at the lateral surfaces. c) σ_x map of CS2 calculated by SB using the subsurface maxima instead of XRD results.

from those values measured in B–E coupons. This difference may suggest that the heat accumulation occurring at the last layers^[38] of the top region induces an intrinsic stress relaxation and/or a localized solute concentration variation. This is, however, subject for future work.

3. Conclusions

To conclude, we propose that the combination of ND and laboratory XRD can well be used to map the RS field in LPBF components and to determine subsurface RS. To this aim, it is proposed that the use of coupon grids extracted from different locations (i.e., need of statistically relevant d_0 measurements) and/or SB conditions are the best alternative nowadays available for quantitative RS analysis in AM parts. Such procedure implies much more work and beamtime than a straightforward analysis applicable to conventional components, but is necessary to tackle the challenges posed by the complexities of AM components in terms of microstructure and defects distribution (see also the study by Fritsch et al.^[40]). Importantly, the possibility of d_0 spatial changes due to chemical and/or textural variations over the volume of a component needs to be evaluated as a function of the AM technique used, as well as the component size.

Acknowledgements

Siemens A.G. is acknowledged for manufacturing and providing the investigated material. The authors thank the ILL for beamtime (experiment 1-02-278 (ref. [29])). Gratitude is also expressed to Sergio Martínez (ILL) for his assistance and guidance during the SALSA experiments and to Mareike Kirstein (BAM) for carrying out the electropolishing.

Open access funding enabled and organized by Projekt DEAL.

Conflict of Interest

The authors declare no conflict of interest.

Data Availability Statement

Data available on request.

Keywords

additive manufacturing, neutron and X-ray diffraction, residual stress analysis, strain-free lattice references, stress balance

Received: July 15, 2021

Revised: August 11, 2021

Published online:

- [1] R. C. Reed, *The Superalloys: Fundamentals and Applications*, Cambridge University Press, Cambridge 2006.
 [2] E. Hosseini, V. A. Popovich, *Addit. Manuf.* **2019**, *30*, 100877.
 [3] W. J. Sames, F. A. List, S. Pannala, R. R. Dehoff, S. S. Babu, *Int. Mater. Rev.* **2016**, *61*, 315.

- [4] T. DebRoy, H. L. Wei, J. S. Zuback, T. Mukherjee, J. W. Elmer, J. O. Milewski, A. M. Beese, A. Wilson-Heid, A. De, W. Zhang, *Prog. Mater. Sci.* **2018**, *92*, 112.
 [5] D. Herzog, V. Seyda, E. Wycisk, C. Emmelmann, *Acta Mater.* **2016**, *117*, 371.
 [6] P. Mercelis, J. P. Kruth, *Rapid Prototyping J.* **2006**, *12*, 254.
 [7] J.-P. Kruth, J. Deckers, E. Yasa, R. Wauthlé, *Proc. Inst. Mech. Eng. Part B: J. Eng. Manuf.* **2012**, *226*, 980.
 [8] J. L. Bartlett, X. Li, *Addit. Manuf.* **2019**, *27*, 131.
 [9] K. Carpenter, A. Tabei, *Materials* **2020**, *13*, 255.
 [10] M. M. Attallah, R. Jennings, X. Wang, L. N. Carter, *MRS Bull.* **2016**, *41*, 758.
 [11] T. Mishurova, K. Artzt, J. Haubrich, G. Requena, G. Bruno, *Metals* **2019**, *9*, 261.
 [12] I. Serrano-Munoz, T. Mishurova, T. Thiede, M. Sprengel, A. Kromm, N. Nadammal, G. Nolze, R. Saliwan-Neumann, A. Evans, G. Bruno, *Sci. Rep.* **2020**, *10*, 14645.
 [13] I. Serrano-Munoz, T. Fritsch, T. Mishurova, A. Trofimov, D. Apel, A. Ulbricht, A. Kromm, R. Hesse, A. Evans, G. Bruno, *J. Mater. Sci.* **2021**, *56*, 5845.
 [14] M. Busi, N. Kalentics, M. Morgano, S. Griffiths, A. S. Tremsin, T. Shinohara, R. Logé, C. Leinenbach, M. Strobl, *Addit. Manuf.* **2021**, *39*, 101848.
 [15] R. Barros, F. J. G. Silva, R. M. Gouveia, A. Saboori, G. Marchese, S. Biamino, A. Salmi, E. Atzeni, *Metals* **2019**, *9*, 1290.
 [16] Y. N. Hu, S. C. Wu, P. J. Withers, J. Zhang, H. Y. X. Bao, Y. N. Fu, G. Z. Kang, *Mater. Des.* **2020**, *192*, 108708.
 [17] M. N. James, *Eng. Fail. Anal.* **2011**, *18*, 1909.
 [18] P. J. Bouchard, in *Encyclopedia of Materials: Science and Technology* (Eds: K. H. J. Buschow, R. W. Cahn, M. C. Flemings, B. Iilschner, E. J. Kramer, S. Mahajan, P. Veysière), Elsevier, Oxford **2001**, pp. 8134–8142.
 [19] P. J. Withers, *Rep. Prog. Phys.* **2007**, *70*, 2211.
 [20] P. J. Withers, M. Preuss, A. Steuwer, J. W. L. Pang, *J. Appl. Crystallogr.* **2007**, *40*, 891.
 [21] M. Strantz, R. K. Ganeriwala, B. Clausen, T. Q. Phan, L. E. Levine, D. C. Pagan, J. Ruff, W. E. King, N. S. Johnson, R. M. Martinez, V. Anghel, G. Rafailov, D. W. Brown, *Addit. Manuf.* **2021**, *45*, 102003.
 [22] Z. Wang, A. D. Stoica, D. Ma, A. M. Beese, *Mater. Sci. Eng. A* **2018**, *714*, 75.
 [23] T. Mishurova, I. Serrano-Munoz, T. Fritsch, A. Ulbricht, M. Sprengel, A. Evans, A. Kromm, M. Madia, G. Bruno, G. Bruno, in *Structural Integrity of Additive Manufactured Materials & Parts* (Eds: N. Shamsaei, M. Seifi), ASTM International, West Conshohocken, PA **2020**, pp. 122–138.
 [24] P. J. Withers, H. K. D. H. Bhadeshia, *Mater. Sci. Technol.* **2001**, *17*, 366.
 [25] T. Mishurova, K. Artzt, J. Haubrich, S. Evsevelev, A. Evans, M. Meixner, I. Serrano-Munoz, I. Sevostianov, G. Requena, G. Bruno, *Metall. Mater. Trans. A* **2020**, *51*, 3194.
 [26] J. Schröder, T. Mishurova, T. Fritsch, I. Serrano-Munoz, A. Evans, M. Sprengel, M. Klaus, C. Genzel, J. Schneider, G. Bruno, *Mater. Sci. Eng. A* **2021**, *805*, 140555.
 [27] I. Serrano-Munoz, A. Ulbricht, T. Fritsch, T. Mishurova, A. Kromm, M. Hofmann, R. C. Wimpory, A. Evans, G. Bruno, *Adv. Eng. Mater.* **2021**, *23*, 2100158.
 [28] G. Bruno, T. Pirling, P. J. Withers, W. Hutt, S. Rowe, *J. Neutron Res.* **2003**, *11*, 235.
 [29] I. Serrano-Munoz, A. Evans, T. Mishurova, T. Pirling, M. Sprengel, Institut Laue-Langevin (ILL), **2019**. <https://doi.org/10.5291/ILL-DATA.1-02-278>.
 [30] ISO21432:2019, <https://www.iso.org/obp/ui/#iso:std:iso:21432:ed-1:v1:en> (accessed: July 2021).

- [31] D. Dye, H. J. Stone, R. C. Reed, *Curr. Opin. Solid State Mater. Sci.* **2001**, 5, 31.
- [32] M. T. Huchings, P. Withers, T. M. Holden, T. Lorentzen, *Introduction to the Characterization of Residual Stress by Neutron Diffraction*, Taylor & Francis, London **2005**.
- [33] P. Fernández-Castrillo, G. Bruno, G. González-Doncel, *Mater. Sci. Eng. A* **2008**, 487, 26.
- [34] G. Bruno, C. Fanara, D. J. Hughes, N. Ratel, *Nucl. Instrum. Methods Phys. Res. Sect. B* **2006**, 246, 425.
- [35] P. Pant, S. Proper, V. Luzin, S. Sjöström, K. Simonsson, J. Moverare, S. Hosseini, V. Pacheco, R. Peng, *Addit. Manuf.* **2020**, 36, 101501.
- [36] Z. Wang, E. Denlinger, P. Michaleris, A. D. Stoica, D. Ma, A. M. Beese, *Mater. Des.* **2017**, 113, 169.
- [37] S. Goel, M. Neikter, J. Capek, E. Polatidis, M. H. Colliander, S. Joshi, R. Pederson, *Mater. Des.* **2020**, 195, 109045.
- [38] T. Mukherjee, W. Zhang, T. DebRoy, *Comput. Mater. Sci.* **2017**, 126, 360.
- [39] D. Ma, A. D. Stoica, Z. Wang, A. M. Beese, *Mater. Sci. Eng., A* **2017**, 684, 47.
- [40] T. Fritsch, M. Sprengel, A. Evans, L. Farahbod-Sternahl, R. Saliwan-Neumann, M. Hofmann, G. Bruno, *J. Appl. Crystallogr.* **2021**, 54, 228.